Identification of coherent structures in cavity flows using stochastic estimation and dynamic mode decomposition

Yang Zhang, Louis Cattafesta

Florida Center for Advanced Aero-Propulsion
Florida State University
Tallahassee, FL
yz12b@my.fsu.edu

Lawrence Ukeiley

Mechanical and Aerospace Engineering
University of Florida
Gainesville, FL

ABSTRACT

This paper identifies coherent structures in cavity flows using Dynamic Mode Decomposition (DMD). Time-resolved (12 kHz) Schlieren is first used to visualize the density gradient field in an open cavity ($L/D = 6$ and $W/D = 3.85$) flow at Mach 0.6. Large-scale vortical structures in the shear layer are observed. The frequencies of the neutrally stable DMD modes match the predicted Rossiter frequencies. The time-resolved velocity field is then estimated using multi-time-delay modified stochastic estimation via non-time-resolved Particle Image Velocimetry snapshots synchronized with time-resolved fluctuating surface pressure measurements. DMD of the resulting estimated time-resolved velocity field also exhibits dominant modes associated with the Rossiter frequencies. The observed coherent structures possess characteristics of traveling waves induced by shear-layer instabilities. Despite the truncation of turbulent kinetic energy in the flow field to obtain the estimated velocity field, the flow dynamics are successfully revealed through this approach.

Introduction

The study of flow over a cavity is a canonical problem. Strong oscillations can arise in weapon and landing-gear bays at moderate-to-high speeds, which can damage the cavity structure and its contents (Heller *et al.* (1971)). Cavity flow can also cause high drag (Gharib & Roshko (1987)). The topic of cavity flows and their control has been studied extensively for decades, and several reviews can be found regarding this topic (Cattafesta *et al.* (2008); Gloerfelt (2009); Lawson & Barakos (2011)). In open cavity flows, an incoming boundary layer separates at the leading edge and forms a free shear layer. Small disturbances in the shear layer amplify due to the well-known Kevin-Helmholtz instability and grow into large vortical structures. When these structures impinge on the trailing edge, they generate an acoustic source that radiates waves upstream. These waves initiate disturbances in the shear layer through a receptivity process. This overall feedback loop can lead to strong peaks and broadband pressure/velocity fluctuations in spectra. The frequencies of these peaks can be predicted using a semi-empirical equation proposed by Rossiter (1964), and these are so-called *Rossiter modes*.

The development of the shear layer is of great importance to the dynamics. Identifying and visualizing the spatial structures elucidate the flow physics (Taira *et al.* (2017)). For instance, Proper Orthogonal Decomposition (POD) can be used to identity the high-energy spatial structures (Berkooz *et al.* (1993)), and furthermore a reduced-order model can be constructed to model the system (Pinnau (2008)). However, POD modes captured from non-time-resolved PIV lack temporal dynamical information of the flow field. In order to obtain the full dynamics, time-resolved data are generally required. Dynamic Mode Decomposition can be performed on the time-resolved data to extract the energetic coherent structures of the flow field associated with a particular frequency (Rowley *et al.* (2009); Schmid *et al.* (2010)). Schmid (2010) recommends the sampling rate be three times that of the Nyquist criterion when performing conventional DMD. This can easily exceed the limitation of current data acquisition hardware (e.g. cameras and lasers in PIV) for measuring flow fields with characteristic frequencies on the order of 1 kHz. The hardware that satisfy the sampling rate can be extremely expensive or may not exist currently. Time-resolved Schlieren is a less costly way to visualize the entire flow field than time-resolved PIV, albeit in an integrated sense along the optical path. In this work, we use a high-speed camera (12 kHz) in a z-type Schlieren system to capture the cavity flow field at Mach 0.6. DMD is performed on 500 snapshots to identify the coherent structures in the density gradient flow field.

A numerical simulation can also provide a time-resolved flow field. However, high-fidelity simulations at high $Re_D(O(10^5))$ are generally prohibitive. An alternative way to obtain the time-resolved velocity field is to take advantage of Stochastic Estimation (SE) to reconstruct a reduced-order time-resolved flow field. The non-time-resolved PIV data and time-resolved flow property are unconditional variables acquired synchronously that are used to estimate the conditional time-resolved velocity field via SE (Adrian (1979)). SE has been developed and applied over the years. Murray & Ukeiley (2003) compared the reconstructed flow fields from linear Stochastic Estimation (LSE) and quadratic Stochastic Estimation (QSE) in the cavity flow. Tinney *et al.* (2006) introduced spectral-based LSE to estimate flow qunatities in the frequency domain. Durgesh & Naughton (2010) applied both single-time-delay (STD) and multi-time-delay (MTD) LSE based on non-time-resolved POD temporal coefficients and time-resolved pressure measurements in the near wake flow. Tu *et al.* (2013) improved the estimate from MTD-mLSE with a Kalman filter. In addition, SE in its causal form can predict the flow field in the future, which can be beneficial in the application of closed-loop control (Ukeiley *et al.* (2008)). Therefore, we apply MTD-mLSE to estimate the time-resolved flow field using low frequency sampled PIV and time-resolved unsteady pressure measurements. This enables the application of the DMD algorithm on the reconstructed data to reveal, study and compare the dynamically important structures associated with the Rossiter frequencies in the velocity field with those of the measured time-resolved density gradient field.

The paper is organized as follows. The methodology section describes the experimental setup and mathematical analysis, followed by the results and discussion. Finally, conclusions are offered.

METHODOLOGIES

Facility and Cavity Model

The experiments are performed in the Pilot Wind Tunnel facility located at the Florida Center for Advanced Aero-Propulsion at the Florida State University. The stagnation pressure, p_0, is measured by a 50 psi absolute pressure transducer via a pitot tube lo-

cated inside the settling chamber. The stagnation temperature, T_0, is measured by a resistance temperature detector (RTD) inserted into the settling chamber. The static pressure, p_s, is measured using a 15 psi absolute pressure transducer via a pressure tap on the sidewall upstream of the cavity model. Wind tunnel flow conditions are monitored and controlled through a LabVIEW program. As shown in Figure 1, the origin of the coordinate system is fixed at the middle of the cavity leading edge. The rectangular cavity model has a dimension of $L/D = 6$ and $W/D = 3.85$ with $D = 26.4$ mm. The incoming boundary layer thickness at the cavity leading edge, δ_0/D, is approximately 0.16 with a shape factor of 1.44 at Mach 0.6. The cavity model is assembled with an acoustically-treated ceiling opposite to the cavity opening. More details about the facility and model are provided in Zhang (2017).

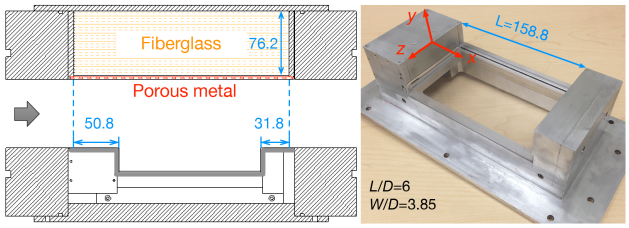

Figure 1: Schematic of the cavity model (units are in mm).

Particle Image Velocimetry and Unsteady Pressure Coupling Measurements

Two-component Particle Image Velocimetry (PIV) is performed to obtain the streamwise flow field on the $z = 0$ center plane. A double-pulse Evergreen Nd:YAG laser (EVG00200) fires the laser pulses at a repetition rate of 15 Hz. The collimated beam travels through a series of optics to pass through the transparent cavity floor forming a laser sheet with a thickness of approximately 1.5 mm, which illuminates sub-micron particles introduced into the flow from the upstream pipe of the stagnation chamber. Two Imager sCMOS cameras (2560×2160 pixels), each equipped with a Nikon Micro-Nikkor 55 mm 1:2.8 lens and a 532 nm band-pass filter, are oriented with their optical axes normal to the laser sheet. The two cameras have an overlapped view at the center of the cavity. Calibration is performed using a customized 2-D dot pattern. Data processing is performed using DaVis 8.3.1. The resulting spatial resolution is approximately 2.8 vectors/mm.

A transparent cavity floor is machined for installing 9 XCQ062 and XCS062 (5 to 15 psid) Kulite sensors with a XT190 (25 psia) Kulite sensor located on the middle of the aft wall. All of the sensors on the floor are shifted off the centerline to avoid blockage of the laser sheet in the PIV measurement. For surface fluctuating pressure measurements, a NI PXI 1031 and three NI 4062 acquire the data at a maximum sample rate of 204.8 kHz for 15 seconds per PIV run. The PIV and unsteady pressure measurements are synchronized via post-processing, and laser pulses are captured using a Scientech photo-diode with the pressure data simultaneously. Details of the experiments are provided in Zhang (2017).

The frequency of Rossiter modes are predicted using the modified Rossiter equation given by Heller *et al.* (1970):

$$St = \frac{fL}{U_\infty} = \frac{n-\alpha}{1/\kappa + Ma_\infty/\sqrt{1+(\gamma-1)Ma_\infty^2/2}}, \tag{1}$$

where the phase lag, α, is 0.38 as in Rossiter (1964), and κ is 0.65, and $n = 0, 1, 2, \ldots$ is the Rossiter mode index.

Schlieren Imaging

A modified z-type Schlieren setup is used to visualize the density gradient in the y-direction in this study. The detailed setup is provided in Zhang (2017).

Multi-Time-Delay modified Linear Stochastic Estimation (MTD-mLSE)

Stochastic Estimation was first introduced by Adrian (1979) to study the turbulent flow and has undergone significant development over the years. Conditional flow properties can be estimated using unconditional flow properties, denoted as $\tilde{u} = \langle u|p\rangle$, where $\tilde{u}$ is the conditional average of u given the unconditional measurement p, which leads to a least-mean-square error estimate of u. Taylor expansion of the stochastic estimation is

$$\tilde{a}_i = \langle a_i|p_k\rangle \approx A_{ij}p_j + B_{ijk}p_jp_k + \cdots, \tag{2}$$

where a_i is the ith POD coefficient, and p_j is the jth probe measurement, and $\tilde{a}$ is the conditional estimate. The coefficients $(A_{ij}, B_{ijk}, \cdots)$ are obtained by minimizing the mean square error $(\langle(\tilde{a}(t) - a(t))^2\rangle)$ of the estimation.

MTD-mLSE is introduced by Durgesh & Naughton (2010) to estimate a conditional variable using information from multi-time-delays of unconditional variables. Keeping just the linear term in Equation 2, MTD-mLSE has the following form

$$\tilde{a}_i(t) = \sum_{n=-m}^{n=m}\sum_{j=1}^{K} A_{ij}p_j(t - \tau_n - \tau_0), \tag{3}$$

where $\tau_n = n(1/f_s)$, $1/f_s$ indicates a time step in the pressure measurements, and τ_0 is the nominal lead or lag time. To minimize the mean square error, the linear coefficients A_{ij} can be calculated using

$$[A_i] = [\overline{PP}]^{-1}[\overline{a_iP}]. \tag{4}$$

Here, $\overline{PP}$ is the auto/cross correlation matrix of unsteady pressure measured by different sensors, and $\overline{a_iP}$ is the cross-correlation vector between the ith POD temporal coefficient and the unsteady pressure sensors.

Dynamic Mode Decomposition

The DMD algorithm applied in the current study is based on Algorithm 1 in Tu *et al.* (2014). The procedure is summarized here. An operator A_{DMD} is defined as

$$A_{DMD} = YX^\dagger \tag{5}$$

where X and Y are data matrices containing snapshots of flow that are separated by one sample interval $[\boldsymbol{z_1}, \boldsymbol{z_2}, \cdots, \boldsymbol{z}_{m-1}]$ and $[\boldsymbol{z_2}, \boldsymbol{z_3}, \cdots, \boldsymbol{z}_m]$, respectively, and $X^\dagger$ denotes the *Moore-Penrose pseudoinvese* of X. The SVD of X is

$$X = USV^*, \tag{6}$$

where V^* denotes the conjugate transpose of V. To calculate the eigenvalues and eigenvectors of A_{DMD} more efficiently, A_{DMD} is projected onto the reduced POD basis as

$$\tilde{A}_{DMD} = U^*A_{DMD}U = U^*YVS^{-1}, \tag{7}$$

in which only the first r_{DMD} singular vectors and values are retained in the SVD (full rank if $r_{DMD} = m-1$). We compute the eigenvalues and eigenvectors of $\tilde{A}_{DMD}$ as

$$\tilde{A}_{DMD}\phi = \lambda\phi. \tag{8}$$

The DMD mode corresponding to the DMD eigenvalue λ is then given by

$$\Phi = U\phi \tag{9}$$

The growth rate of the mode is calculated from the eigenvalue λ as $g = \log|\lambda| f_s$, while the frequency is $f = \angle\lambda f_s/(2\pi)$, where f_s is the sampling frequency.

RESULTS AND DISCUSSION

The mean removed velocity fields obtained from the PIV measurements are normalized by U_∞ and used for determining the POD temporal coefficients and spatial modes. The eigenvalues λ from the POD calculation represent the TKE content of each mode, and they are ordered from highest to lowest energy as the mode index increases. The percentage of the sum of the first r modes is calculated using

$$\text{energy}\% = \frac{\sum_{i=1}^{r}\lambda_i}{\sum_{i=1}^{N}\lambda_i}, \tag{10}$$

where the denominator represents the total TKE. The energy fraction as a function of number of modes, and the mode shape of the velocity components of the first three modes are presented in Figure 2.

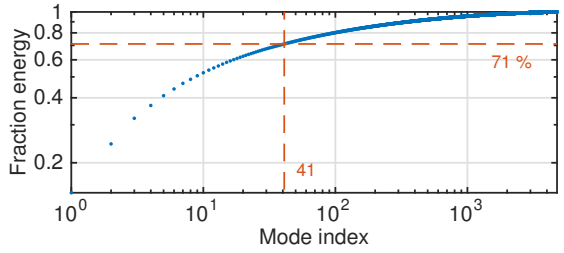

(a) Accumulated energy as a function of the number of modes.

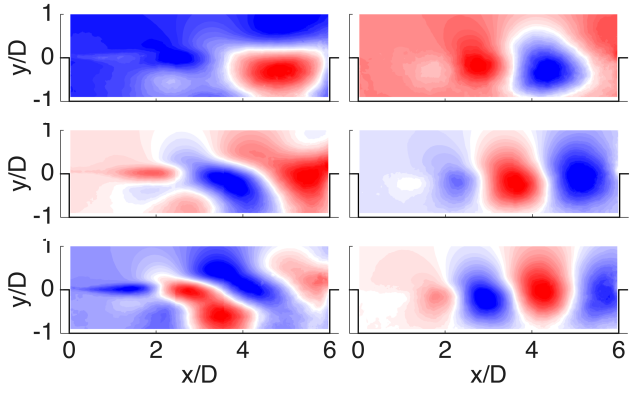

(b) First three POD modes of u' (left column) and v' (right column) components.

Figure 2: Energy fraction and representative POD mode shapes.

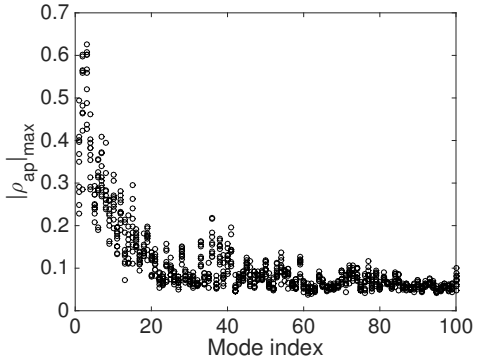

(a) Maximum correlation coefficient magnitude between the POD coefficients and unsteady pressure measured by different sensors as a function of mode index.

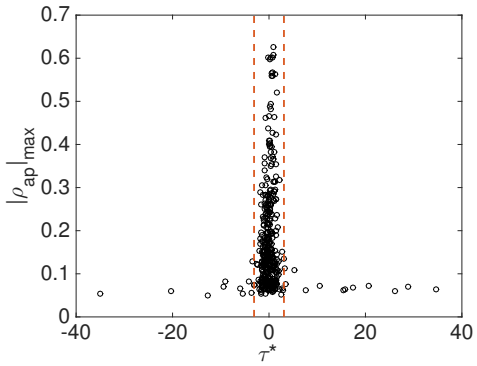

(b) Distribution of maximum correlation coefficient magnitude as a function of τ^*. Dashed lines indicate $\tau^* = -3$ and 3.

Figure 3: Cross-correlation between the POD coefficients and unsteady pressure measured at different locations inside the cavity.

After obtaining the POD temporal coefficients from the velocity snapshots, MTD-mLSE is performed. The surface fluctuating pressure data are down-sampled from 204.8 kHz to 25.6 kHz. The unsteady pressure are normalized by q_∞. A non-dimensional convective time delay is defined as $\tau^* = \tau U_\infty/L$. The maximum of the absolute value of the cross-correlation coefficients between the POD temporal coefficients and unsteady pressure at different locations are shown in Figure 3a. As the mode index increases, the correlation deteriorates. By using only POD modes with high correlation, the first 41 modes are retained, which contain approximately 71% of the total TKE. The distribution of the maximum absolute value of the correlation coefficient between the first 41 modes and 10 sensors over a wide τ^* range is plotted in Figure 3b. It is clear that high correlations only occur within a narrow τ^* band from -3 to 3.

From the standpoint of statistics, an overfitted model has poor predictive performance, as it overreacts to using data with low correlation and noise. The model can also suffer if the τ^* range is too wide. To implement the estimation procedure more carefully, a 2-fold cross-validation process is performed to evaluate the performance (Mosteller & Tukey (1968)). The total number of $2N = 4772$ snapshots is split into two groups; the first N snapshots form the training set, and the next N form the validation set. MTD-mLSE is performed on the training set for a specified τ^* range and is then used to estimate the snapshots reconstructed from the same 41 POD training modes in the validation set. The difference between the resulting estimate and the reduced-order POD model with 41 modes is used to quantify the rms error averaged over the entire domain and N snapshots (Equation 11). These steps are repeated for different τ^* ranges. The entire procedure is performed again with the two

sets swapped, and the combined error is the rms error of test 1 and test 2.

$$e_{\boldsymbol{u}} = \sqrt{\frac{1}{N}\sum_{i=1}^{N}\frac{\|\tilde{\boldsymbol{u}}_i - \boldsymbol{u}_i\|_2^2}{\|\boldsymbol{u}_i\|_2^2}}. \tag{11}$$

where $\boldsymbol{u}$ represents the velocity vector. Because $\pm\tau^*$ is symmetrically applied about $\tau_0 = 0$, $\tau^*_{\text{half}} = 0.5(\tau^*_{\max} - \tau^*_{\min})$ for a specific τ^* range. The rms error of the estimated velocity components versus τ^*_{half} is presented in Figure 4. The error decreases initially with increasing of τ^* range. However, the error reaches a minimum and then increases for a larger τ^* range. This shows the estimation is not necessarily improved with a larger τ^* range. Therefore, the optimal τ^* range for MTD-mLSE is thus determined to be [-0.34,0.34].

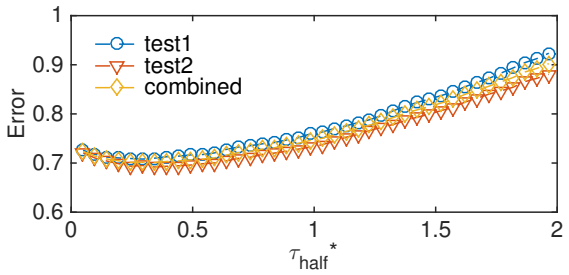

Figure 4: Estimation error in MTD-mLSE obtained via a 2-fold cross validation process, where τ^*_{half} denotes half of the range of τ^* used in the estimation process.

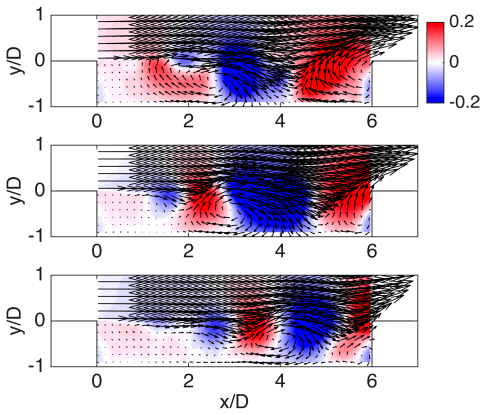

Figure 5: A successive series of reconstructed flow fields showing v-velocity contours overlaid with velocity vectors using MTD-mLSE. The time interval $\Delta\tau^*$ between each successive flow field is 0.393.

After the cross validation, MTD-mLSE is applied on the total number of snapshots to reconstruct the time-resolved velocity fields. A successive series of reconstructed flow fields are provided in Figure 5. From the v-velocity contour, it is clear that the convection of the flow is successfully reconstructed. From the vectors, the recirculation regions are also captured. These flow features are similar to those found using QSE in Ukeiley & Murray (2005).

Before applying DMD on the reconstructed time-resolved velocity fields, the DMD algorithm is first performed on the time-resolved Schlieren images. A fast Fourier Transform is applied on 5000 Schlieren images to estimate the power spectrum of the data set, and the Euclidean norm of the spectrum of the flow field at each frequency is computed and shown in Figure 6. The frequency of these high level peaks are quite consistent with the predicted Rossiter frequencies. This indicates that the dynamics of the spanwise averaged flow field is well captured in the density-gradient, which implies that the dynamics of the data can be further analyzed using DMD.

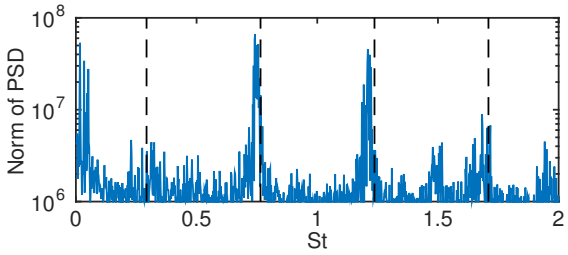

Figure 6: Spectrum of the Schlieren image set. The dashed lines indicate the predicted Rossiter frequencies from Equation 1.

The standard DMD algorithm is subsequently performed on 500 successive time-resolved Schlieren images. As shown in Figure 7, all of the eigenvalues of the DMD modes are located on the unit circle, corresponding to purely oscillatory modal. In the Schlieren images, the disturbances in the shear layer that grow into large-scale vortical structures are due to the Kelvin-Helmholtz instability, but their growth is ultimately attenuated by nonlinear saturation. Therefore, the modes observed in the experiments are expected to have eigenvalues on the unit circle (saturation state). Except for the mode at $St = 0$ corresponding to the mean flow, the frequencies of the high-amplitude modes (Figure 7) are consistent with the predicted Rossiter frequencies, as listed in Table 1. The mode shapes are presented in Figure 8; the structures are formed in pairs on both sides of the shear layer across the cavity opening, which are consistent with the modal shapes of the density gradient field observed by Kegerise (1999) using phase-locked quantitative Schlieren. This indicates that the modes of linear approximated model exhibit good agreement with the direct measurements of the nonlinear saturated system (Rowley *et al.* (2009)).

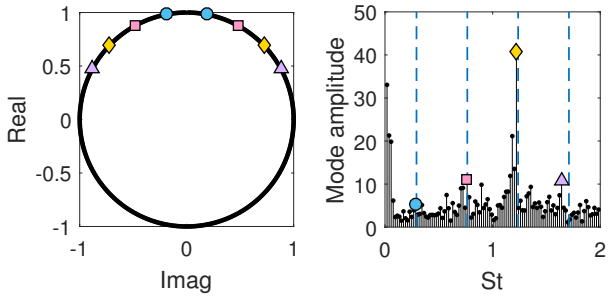

Figure 7: Results of the DMD analysis of the time-resolved Schlieren images. Colored markers indicate the DMD modes corresponding to the Rossiter frequencies.

After the initial test with the density gradient fields, DMD is subsequently applied on the estimated time-resolved velocity fields. Recalling that only the first 41 POD modes are used for estimating

Table 1: Comparison of mode *St* obtained by different methods.

Rossiter modes	I	II	III	IV
Predicted frequency	0.30	0.76	1.24	1.71
PSD of images	0.31	0.75	1.22	1.69
DMD	0.29	0.76	1.22	1.64

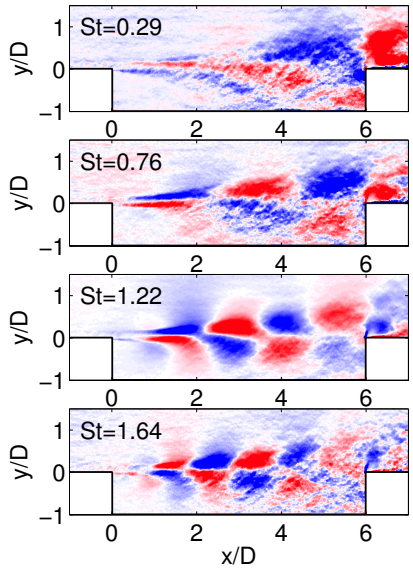

Figure 8: High-energy coherent structures of the density gradient field associated with different frequencies.

the time-resolved flow field through MTD-mLSE, the DMD operator A_{DMD} is projected on the low-rank POD basis containing the first 41 modes. The distribution of eigenvalues of standard DMD on the velocity fields is provided in Figure 9. Because all Rossiter modes are not globally observed in the reconstructed velocity spectra, the peaks split near the estimated Rossiter frequencies. Based on the predicted Rossiter modes, the DMD modes are selected as the colored markers. Unlike the Schlieren case in which all eigenvalues are located on the unit circle, the dominant modes are lightly damped, likely due to the 71% TKE content in the truncated model.

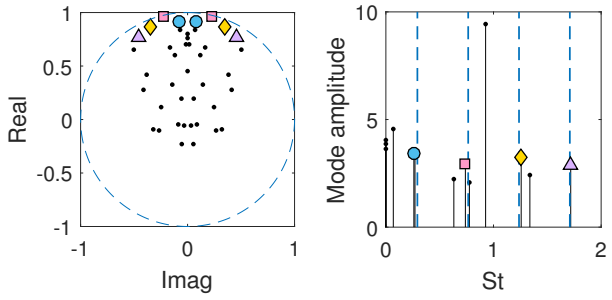

Figure 9: Results of the DMD analysis of the estimated time-resolved velocity field. Colored markers indicate the DMD modes corresponding to the Rossiter frequencies.

Then, the most energetic modal structures of the velocity components and the spanwise vorticity fluctuations are extracted and shown in Figure 10. The mode shapes of u' and v' exhibit quite different flow structures: the modes of the streamwise velocity fluctuations (except the first mode) are similar to the modes obtained from the Schlieren images that produce structured pairs located on both sides of the shear layer, and the mode shapes of the normal velocity fluctuations are similar to the POD modes of the v-velocity component. The mode shape of the spanwise vorticity fluctuations exhibits some other different flow structures. A pair of lobes are located on both sides of cavity opening at $y/D = 0$. As the mode index increases, the scale of these structures decreases. These structures are localized in the region of the shear layer, unlike the more global-like distribution of the modes of the u' and v' components. These flow features are all related to traveling waves induced by the Kelvin-Helmholtz instability.

For the first mode, the wavelength is larger than the cavity length. Therefore, a complete wave pattern cannot be visualized in the current study due to the limited domain size. A larger domain extending farther downstream of the cavity trailing edge is likely required to capture this structure. Furthermore, additional evidence that the first mode is not accurately captured lies in two comparable mode amplitudes around the first Rossiter frequency in Figure 10. However, the flow structures associated with higher Rossiter frequencies are captured by DMD.

CONCLUSIONS

Time-resolved Schlieren imaging is conducted to capture the integrated $L/D = 6$, $W/D = 3.85$ cavity flow at Mach 0.6. The FFT of 5000 snapshots is computed, and the high-level peaks in the norm of the spectra correspond to the predicted Rossiter frequencies. Standard DMD analysis is performed on 500 successive snapshots, and dynamically important structures are successfully identified and visualized. The frequency of high-amplitude modes are consistent with Rossiter modes, which implies the dominant two-dimensional dynamics are captured in the density-gradient field. The structures form in pairs on both sides of the shear layer, and the length scale decreases with increasing frequency.

Synchronous 15 Hz PIV and time-resolved unsteady surface pressure measurements from 10 probes inside the cavity are conducted to establish the correlation between velocity fields and surface fluctuating pressure. MTD-mLSE is performed based on the first 41 POD modes containing approximately 71% of the TKE to estimate the time-resolved flow field. The method successfully reconstructs the convective flow motion and recirculation regions. DMD is then applied on the estimated time-resolved flow fields. The DMD modes corresponding to the Rossiter frequencies are identified. The dynamic modes of the velocity components and the spanwise vorticity fluctuations are presented, showing characteristic structures of traveling waves induced by the Kelvin-Helmholtz instability.

As a reduced-order approach, POD modes with approximately 30% TKE have been filtered, and the potential contribution of these modes to the flow dynamics warrants further study. Despite this deficiency, the current study provides a method to study the pertinent dynamics of high-speed cavity oscillations.

ACKNOWLEDGMENTS

This research was supported by the U.S. Air Force Office of Scientific Research (Award Number FA9550-13-1-0091, Program Manager: Dr. Douglas Smith). The authors would like to thank Yiyang Sun, Kunihiko Taira and Eric Deem for their feedback to this paper.

REFERENCES

Adrian, Ronald J. 1979 Conditional eddies in isotropic turbulence. *The Physics of Fluids* **22** (11), 2065–2070.

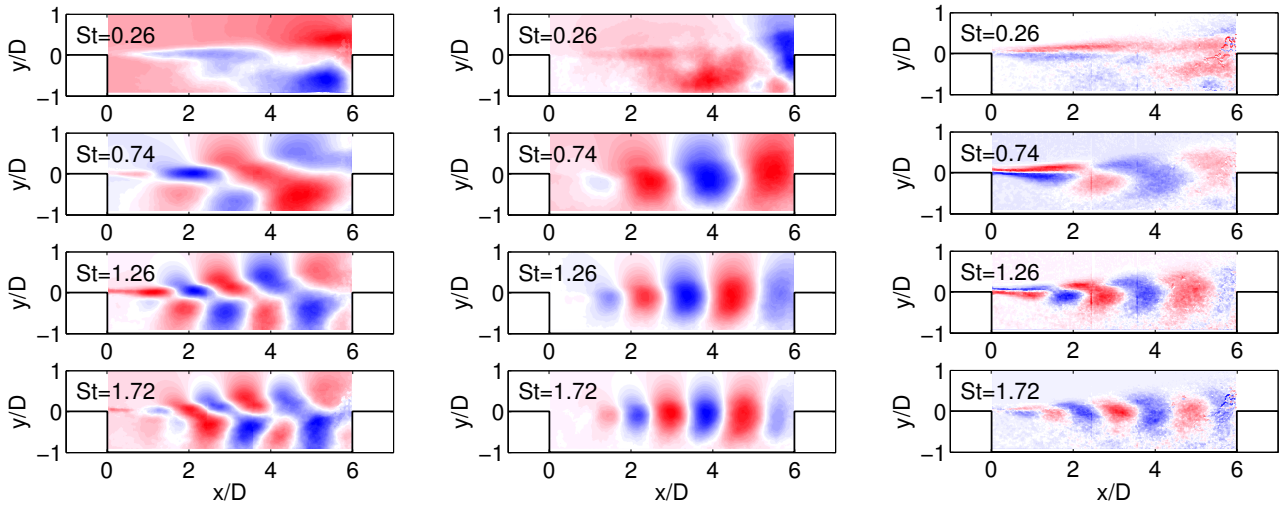

(a) u' (b) v' (c) ω_z'

Figure 10: Mode shapes (real part) corresponding to the first 4 Rossiter frequencies from top to bottom obtained by standard DMD.

Berkooz, Gal, Holmes, Philip & Lumley, John L. 1993 The proper orthogonal decomposition in the analysis of turbulent flows. *Annual Review of Fluid Mechanics* **25** (1), 539–575.

Cattafesta, Louis, Song, Qi, Williams, David R., Rowley, Clarence W. & Alvi, Farrukh S. 2008 Active control of flow-induced cavity oscillations. *Progress in Aerospace Sciences* **44** (78), 479 – 502.

Durgesh, V. & Naughton, J. W. 2010 Multi-time-delay lse-pod complementary approach applied to unsteady high-reynolds-number near wake flow. *Experiments in Fluids* **49**, 571–583.

Gharib, M. & Roshko, A. 1987 The effect of flow oscillations on cavity drag. *Journal of Fluid Mechanics* **177**, 501–530.

Gloerfelt, Xavier 2009 Cavity noise. In *J. Anthoine, J. Christophe (Eds) VKI lecture series 2009-03, aerodynamic noise from wall-bounded flows*. Von Karmen Institute for Fluid Dynamic, Brussels.

Heller, H. H., Holmes, D. G. & Covert, E. E. 1970 Flow-induced pressure oscillations in shallow cavities AFFDL-TR-70-104.

Heller, H. H., Holmes, D. G. & Covert, E. E. 1971 Flow-induced pressure oscillations in shallow cavities. *Journal of Sound and Vibration* **18** (4), 545 – 553.

Kegerise, Michael Aaron 1999 An experimental investigation of flow-induced cavity oscillations. PhD thesis, Syracuse University.

Lawson, S.J. & Barakos, G.N. 2011 Review of numerical simulations for high-speed, turbulent cavity flows. *Progress in Aerospace Sciences* **47** (3), 186 – 216.

Mosteller, F. & Tukey, J 1968 Data analysis, including statistics. In *Revised Handbook of Social Psychology* (ed. G. Lindzey & E. Aronson), , vol. 2, pp. 80–203. Addison Wesley.

Murray, Nathan E. & Ukeiley, Lawrence S. 2003 Estimation of the flowfield from surface pressure measurements in an open cavity. *AIAA Journal* **41** (5), 969–971.

Pinnau, René 2008 *Model Reduction via Proper Orthogonal Decomposition*, pp. 95–109. Berlin, Heidelberg: Springer Berlin Heidelberg.

Rossiter, J. E. 1964 Wind-tunnel Experiments on the Flow over Rectangular Cavities at Subsonic and Transonic speeds. *Tech. Rep.*. Aeronautical Research Council Reports and Memoranda, no. 3438.

Rowley, Clarence W., Mezić, Igor, Bagheri, Shervin, Schlatter, Philipp & Henningson, Dan S. 2009 Spectral analysis of nonlinear flows. *Journal of Fluid Mechanics* **641**, 115–127.

Schmid, Peter J. 2010 Dynamic mode decomposition of numerical and experimental data. *Journal of Fluid Mechanics* **656**, 5–28.

Schmid, P. J., Li, L., Juniper, M. P. & Pust, O. 2010 Applications of the dynamic mode decomposition. *Theoretical and Computational Fluid Dynamics* **25** (1), 249–259.

Taira, Kunihiko, Brunton, Steven L., Dawson, Scott T. M., Rowley, Clarence W., Colonius, Tim, McKeon, Beverley J., Schmidt, Oliver T., Gordeyev, Stanislav, Theofilis, Vassilios & Ukeiley, Lawrence S. 2017 Modal analysis of fluid flows: An overview. *AIAA Journal* In review.

Tinney, C. E., Coiffet, F., Delville, J., Hall, A. M., Jordan, P. & Glauser, M. N. 2006 On spectral linear stochastic estimation. *Experiments in Fluids* **41** (5), 763–775.

Tu, Jonathan H., Griffin, John, Hart, Adam, Rowley, Clarence W., Cattafesta, Louis N. & Ukeiley, Lawrence S. 2013 Integration of non-time-resolved piv and time-resolved velocity point sensors for dynamic estimation of velocity fields. *Experiments in Fluids* **54** (2), 1429.

Tu, Jonathan H., Rowley, Clarence W., Luchtenburg, Dirk M., Brunton, Steven L. & Kutz, J. Nathan 2014 On dynamic mode decomposition: Theory and applications. *Journal of Computational Dynamics* **1** (2), 391–421.

Ukeiley, Lawrence & Murray, Nathan 2005 Estimation of Time Dependent Flow Properties in an Open Cavity. In *ASME 2005 Fluids Engineering Division Summer Meeting*, pp. 335–344. ASME.

Ukeiley, Lawrence, Murray, Nathan, Song, Qi & Cattafesta, Louis 2008 *Dynamic Surface Pressure Based Estimation for Flow Control*, pp. 183–189.

Zhang, Yang 2017 Three dimensional control of high-speed cavity flow oscillations. PhD thesis, Florida State University.

Zhang, Yang, Sun, Yiyang, Arora, Nishul, Cattafesta, Louis, Taira, Kunihiko & Ukeiley, Lawrence 2015 Suppression of Cavity Oscillations via Three-Dimensional Steady Blowing. Dallas, TX, AIAA 2015-3219.